



HAL
open science

Investigation of steel corrosion in MX80 bentonite at 120°C

Hélène Lotz, Charly Carrière, Christian Bataillon, Emmanuel Gardes, Isabelle Monnet, Eddy Foy, Michel L Schlegel, James J Dynes, Delphine D. Neff, Florence F. Mercier-Bion, et al.

► **To cite this version:**

Hélène Lotz, Charly Carrière, Christian Bataillon, Emmanuel Gardes, Isabelle Monnet, et al.. Investigation of steel corrosion in MX80 bentonite at 120°C. *Materials and Corrosion / Werkstoffe und Korrosion*, 2021, 71 (1-2), pp.120-130. 10.1002/maco.202011777 . cea-02931494

HAL Id: cea-02931494

<https://cea.hal.science/cea-02931494v1>

Submitted on 11 Dec 2020

HAL is a multi-disciplinary open access archive for the deposit and dissemination of scientific research documents, whether they are published or not. The documents may come from teaching and research institutions in France or abroad, or from public or private research centers.

L'archive ouverte pluridisciplinaire **HAL**, est destinée au dépôt et à la diffusion de documents scientifiques de niveau recherche, publiés ou non, émanant des établissements d'enseignement et de recherche français ou étrangers, des laboratoires publics ou privés.

Title: Investigation of steel corrosion in MX80 bentonite at 120°C

Running title: Steel corrosion in MX80 bentonite at 120°C

Hélène Lotz¹, Charly Carrière¹, Christian Bataillon², Emmanuel Gardes³, Isabelle Monnet³,
Eddy Foy¹, Michel L. Schlegel⁴, James J. Dynes⁵, Delphine Neff¹, Florence Mercier¹,
Philippe Dillmann¹

¹*Université Paris-Saclay, CEA, CNRS, NIMBE, 91191, Gif-sur-Yvette, France*

²*CEA, Des – Service de Corrosion et de Comportement des Matériaux dans leurs Environnement (SCCME), Université Paris-Saclay, 91191, Gif sur Yvette, France*

³*Centre de Recherches sur les Ions, les Matériaux et la Photonique (CIMAP), Normandie Université, CEA, CNRS, UCBN, ENSICAEN, F-14070 Caen cedex5 France*

⁴*Université Paris-Saclay, CEA, Service d'Études Analytiques et de Réactivité des Surfaces, 91191, Gif-sur-Yvette, France*

⁵*Canadian Light Source Inc., University of Saskatchewan, Saskatoon, SK S7N 0X4, Canada*

Corresponding author: Hélène Lotz, *Université Paris-Saclay, CEA, CNRS, NIMBE, 91191, Gif-sur-Yvette, France, helene.lotz@cea.fr*

Abstract

Corrosion experiments were performed on two metallic substrates, a ferritic-pearlitic steel (P285NH) and a ferritic one (Armco), in silicate environment during 30 days at 120°C. Corrosion products were characterized in terms of morphology (SEM, TEM), composition (EDS) and structure (μ -Raman, SAED, XANES). Results show a nanometric inner layer made of compact and adherent nano-crystallized magnetite with, locally a thickness up to several micrometers due to the metal microstructure. An outer layer of Fe-rich phyllosilicate, smectite and serpentine, more porous than the inner one and poorly adherent is observed around both samples.

Key words

Steel, anoxic corrosion, MX80 bentonite, multiscale analysis, magnetite, iron silicate,

Introduction

Deep geological disposal is being studied in many countries as a long-term (>10 000 years) answer to the management of high-level radioactive waste [1]. The host rocks are selected according to their properties and their availability in each country. In France, a Callovo-Oxfordian claystone (Cox) located 500 m deep in the east of the Paris basin, is currently being investigated. The French National Radioactive Waste Management Agency (Andra) plans to confine the radionuclides in Cox using a multi-barrier system made up of a glass matrix embedded in a stainless steel container, confined in a carbon steel overpack [1,2]. These waste packages would be stored in boreholes lined with steel tubes in the clay host rock. After closure of the system, the packages are expected to experience mostly anoxic conditions. The low permeability of the clay host could delay the water ingress in contact with the packages.

The longevity of such a storage system is assessed by predictive models based on identified long-term corrosion mechanisms of the metallic containers. For decades, several studies have examined steel generalized corrosion in argillite media and in carbonated clay pore water [3–12]. In the geochemical conditions of the repository, i.e. an anoxic and carbonated environment, the formation of Fe-rich stable phases, namely iron oxides, carbonates, sulphates and silicates was observed [13,14]. The Corrosion Product Layers (CPL) can be described as follows: an internal magnetite oxide layer, an external layer consisting of Fe-rich phyllosilicates sometimes with iron carbonates, and a transformed medium layer with iron carbonate. Each phase has its own physico-chemical properties influencing the corrosion mechanisms of steel and the alteration rate. For example, the presence of an oxide layer at the metal/corrosion product layer (M/CPL) interface could decrease the corrosion rate [15]. Moreover, studies from the oil and gas industry demonstrated that carbonate corrosion products also slow down the corrosion rate by moderating ion diffusion through the CPL [16]. On the contrary, formation of non-expansive, or swelling Fe-rich silicates, such as serpentine or smectite respectively, was shown to change the permeability properties around the steel surface [17].

Studies performed on Iron / Clay interactions without carbonate buffer have shown the formation of magnetite and Fe-rich silicate [18–20]. These studies were performed in **chloride** solution or distilled water at 80-90°C on powder in order to maximize the contact surfaces, and aimed to understand the processes of clays destabilization (Cox without carbonate minerals, MX80, montmorillonite, saponite...) by iron. However, they have not scrutinized the metallic interface as well as the CPL layout. Yet, more investigations focusing on that issue are needed

1
2
3 to understand the interplay between silicate transformation and iron corrosion mechanism, like
4 the formation (or not) of a protective oxide interfacial layer at the M/CPL interface.
5
6

7 This study considers steel corrosion in MX80 bentonite and in Cox porewater without
8 carbonate minerals to simulate a compact silicate environment in absence of a carbonate buffer.
9 Two types of metallic substrates are studied, a ferritic-pearlitic steel and a ferritic one, in order
10 to investigate potential influence of the steel microstructure and composition on the corrosion
11 behaviour. The morphology, composition and structure of the corrosion products are
12 determined using a multiscale approach (macro-micro-nano). Their properties are discussed and
13 the role of the corrosion product layers is explained.
14
15
16
17
18
19

20 **Materials and methods**

21
22 In this work, a steel, P285NH, and a pure iron, Armco, were studied. Their compositions
23 are given in Table 1. P285NH is a ferritic-pearlitic steel which microstructure is made of two
24 elements: α -Fe grains and of pearlite grains formed by a succession of α -Fe and cementite Fe_3C
25 lamellas. Armco is a pure ferrite containing only α -Fe grains. The comparison with these two
26 steels is essential to highlight the effect of cementite on the corrosion processes. The metallic
27 coupons were mechanically polished under ethanol with SiC paper (up to grade 4000). Between
28 each polishing grade, samples were ultrasonically cleaned for 2 min in ethanol to remove SiC
29 grains.
30
31
32
33
34
35

36
37 The corrosion experiment was performed in an autoclave at 120°C for 30 days. This
38 high temperature was chosen in order to increase the reaction kinetics. The samples were
39 simultaneously immersed in Cox pore water synthetic solution mixed with 30% wt. of MX80
40 bentonite to simulate a simplified compact clay environment. Compositions of the Cox
41 synthetic pore water without carbonated compounds [21] and MX80 bentonite [14] are given
42 in Table 2 and 3, respectively. After sample immersion, the autoclave was evacuated to remove
43 oxygen and reach anoxic conditions. Upon completion of the experiment, the samples were
44 dried using a stream of dry air and then stored under primary vacuum.
45
46
47
48
49
50

51 Prior to analyses, samples were embedded in epoxy resin (EpoFix, Struers) then cut with
52 a precision diamond saw (Minitom, Struers). The cross-sections were ground with SiC paper
53 (up to grade 4000) under ethanol, and then polished with 1 μm diamond paste on a velvet disk.
54 Cross-section were etched with Nital in order to reveal the metal microstructure in the light of
55 the corrosion products. Observation of the corrosion systems were performed both before and
56 after etching.
57
58
59
60

1
2
3 Field Emission Gun–Scanning Electron Microscope (JEOL SEM 7001F) was used to
4 investigate the interfaces in backscattered electron (BSE) and secondary electron (SE) modes.
5 The scanning electron microscope (SEM) is coupled to a silicon drift detector (SDD) to obtain
6 the elemental composition by Energy Dispersive X-ray Spectroscopy (EDS). Analyses were
7 performed at 10 kV on metallized samples. Aztec software, developed by Oxford Instruments
8 was used for data acquisition and for data treatment.
9

10
11
12
13
14 Raman analyses were performed on an Invia Renishaw microspectrometer equipped
15 with a frequency-doubled Nd-YAG green laser (532 nm wavelength) and with a high groove
16 density grating (2400 gr/mm) associated with a coupled charge device (CCD) detector. The
17 beam was focused using a Leica optical microscope. At 50x magnification the beam lateral size
18 is 1.2 μm and has a probed depth of about 1 μm . Laser power was filtered at 0.1 mW to avoid
19 any damage of the corrosion products. The spectrometer energy was calibrated by setting the
20 Raman line of a silicon wafer to 520.5 cm^{-1} . Spectra were acquired using Wire 3.4 software
21 with a resolution of 2 cm^{-1} between 200 and 1200 cm^{-1} and dwell time of 60 s.
22
23
24
25
26
27

28
29 Thin foils (~100 nm and ~1 μm thick) were extracted from the samples to analyse the
30 Metal/Corrosion Product Layer (M/CPL) interface using a SEM coupled with Focused Ga-Ion
31 Beam FEI Nanolab 660. Lamella thinning was performed first using 30 kV Ga ions, followed
32 by final polishing at decreasing energies of 5, 2 and 1 kV to remove damaged and Ga-implanted
33 layers on each side of the lamellas [22], and finally stored in sealed jars under primary vacuum.
34 The 100 nm and 1 μm thick foils were used for transmission electron microscopy (TEM) and
35 Scanning Transmission X-ray Microscopy (STXM) analyses at Si K-edge, respectively.
36
37
38
39
40

41 For TEM analysis, a JEOL 2010 F equipped with a diode EDAX X-ray microanalysis
42 was operated at 200 kV. Complementary Selected Area Electron Diffraction (SAED) as well
43 as dark field imaging on characteristic diffraction spots were used to identify solid phases.
44 Interplanar spacings were calculated with ImageJ software, and then compared to d_{hkl} values
45 from Joint Committee on Powder Diffraction Standards (JCPDS) cards.
46
47
48
49

50 The chemical environment of iron silicates was characterized using synchrotron
51 radiation using STXM at the Si K-edge on the 10ID-A beamline at the Canadian Light Source
52 (CLS). Analyses and data processing, achieved with aXis2000 software, have already been
53 described in the literature [23,24]. Experimental spectra decomposition was done using a least
54 square method with standard reference spectra from a previously created database [22].
55
56
57
58
59

60 Results

1. Corrosion distribution around the metallic samples

The corroded interface can be divided into two parts for both steel nuances (figure 1). Firstly, an inner corrosion product layer (iCP), light grey contrast in the BSE, seems compact and adherent to the metallic surface. Secondly, a discontinuous layer of external corrosion product (eCP) with various darker grey contrasts appears porous and poorly adherent to the iCP. The eCP morphology appears heterogeneous with disjointed chunks. The characterisation of the two corrosion product layers will be presented in the next two paragraphs.

2. Characterization of the iCP

SEM micrographs in SE mode were obtained after metallographic etching of the cross-sections in order to reveal the possible connection between the metallic microstructure and the corrosion products (Fig. 2). A continuous inner layer of 500 nm average thickness (Fig. 2AB) and up to 25 μm locally (Fig. 2CD) in contact with the metal is evidenced for both samples. For P285NH, local corrosion penetrations are commonly observed and can be correlated with the presence of pearlite grains in the metal microstructure (Fig. 2C). However, this is not systematic because some contiguous pearlite grains around the metal are not associated with such local penetrations (Fig. 2A). For Armco, the local penetrations of corrosion products are rarer (three per cross section of diameter 2.5 cm) but deeper (up to 25 μm) than for P285NH and do not seem to be related to the metal microstructure (Fig. 2D).

SEM-EDS investigations of the iCP detected only Fe and O as major elements. Raman spectroscopy was performed on the iCP of both metallic samples. All spectra present an intense band at 669 cm^{-1} with two weaker bands at 550 cm^{-1} and 305 cm^{-1} (Fig. 3), characteristic of magnetite Fe_3O_4 [25].

This magnetite layer was investigated by TEM on thin foils collected on each sample in order to highlight its crystalline properties. Diffraction patterns collected by SAED close to the metal interface confirmed the presence of magnetite (JCPDS 19-0629; Fig. 4A and table 4). Interestingly, the SAED pattern of the magnetite displays almost continuous rings, meaning magnetite domains are small compared to the lateral size of the electron beam. TEM images collected on P285NH (Fig. 4B) and Armco (Fig. 4C) showed that the magnetite grain size is less than 30 nm diameter. Moreover, TEM acquisitions performed at the M/CPL interface indicate that the oxide layer is compact, non-porous at nanoscale and adherent to the metal (Fig. 4C)

3. Characterisation of the eCP

The external CPL appears darker (in BSE mode) than the oxide layer (Fig. 5), suggesting the presence of lighter elements. Besides, corrosion products seem poorly adherent to the metal and appear porous as they are infiltrated with some resin (in black on Fig. 1 and 5). They extend from 40 μm to 60 μm in the clay matrix. EDS measurements (Fig. 5, Table 5) show the presence of mainly Fe and Si containing phase, associated with O, Al and Mg. Interestingly, in the eCP layers of both samples, two Fe-Si-O rich phases with distinct compositions are identified. Firstly, homogeneous concentrations of Fe (17 at.%) and Si (18 at.%), with Al (10 at.%) and Mg (1-1.5 at.%) is compatible the presence of trioctahedral phyllosilicate corresponding to the serpentine group [26] (see points 1 and 3 for P285NH and Armco respectively). Secondly, phases with Si content (21 at.%) higher than Fe (5-6 at.%) with Al (7 at.%) and Mg (1-2 at %) suggest the presence of smectite type minerals (points 2 and 4 for P285NH and Armco respectively) [27]. Due to the weak Raman scattering of these phases, their investigation by Raman spectroscopy was not possible [3]. Hence, High-Resolution Transmission Electron Microscopy (HR-TEM) was used. HR-TEM micrographs revealed foliated aggregates (Fig. 7), compatible with the morphology of phyllosilicate particles [28]. In both eCP, HR-TEM analyses reveal characteristic d_{001} distances of 13 Å (Fig. 6AB) and 7.3 Å (Fig. 6CD), compatible with hydrated smectite and serpentine respectively [29–34].

To assess the local crystallochemical organization of the Fe-Si-O rich phases, and to narrow the iron silicate identification, STXM spectra were collected at the Si K-edge. Reference spectra of MX80 bentonite, montmorillonite and quartz were collected to discriminate iron silicate formed in the present study and silicates from MX80 bentonite (fig. 7A). Two different spectra were obtained in the eCP of both samples, i.e. for P285NH and Armco (Fig. 7B and 7C). The first spectrum (Fig. 7B) presents a major peak at 1846.0 eV (peak A), an oscillation at 1856.3 eV (C) and an additional broad band at 1861.9 eV (D). The second spectrum (Fig. 7C) also displays the A and D contributions at 1846.0 eV and 1861.9 eV respectively, but presents an intense additional shoulder at 1851.4 eV (peak B) and a smaller oscillation at the C position at 1856.6 eV. Note that for the two different spectra, the major peak (A) and the broad band (D) correspond to the Si fourfold coordinated by O and the contribution of neighbouring O respectively [35,36]. The spectrum on Fig. 7A is qualitatively compared with the Si K-edge spectra database collected by Carrière et al. [22]. The presence of the A, C and D contributions identifies the smectite group (excepting saponites), and excludes chlorites, mica and

1
2
3 serpentine-kaolinites [7,22]. The qualitative approach conducted on the second spectrum (Fig.
4 7C) excludes the smectites and the chlorites group, and can promote serpentine group.
5
6

7 Then, these two experimental spectra were decomposed by a linear regression using the
8 reference spectra of selected minerals. The best fits (Fig. 7B and Table 6) are obtained with the
9 combination of only two reference phases: about 90 % of Garfield nontronite, an Fe(III)-rich
10 smectite, and 10 % of amorphous SiO₂. The good quality of the fit is attested with $R^2 = 0.99$
11 and $\chi^2 = 0.01$. Note that the amorphous contribution generated by the amorphization of each
12 face of the FIB foils, during thinning process [3,37], is not the only feature to explain this
13 amorphous part. Indeed the Si: Fe: Al ratio impacts the nontronite crystallinity [38,39].
14 Regarding the other spectra collected in the eCP layer of P285NH and Armco (Fig. 7C), no
15 satisfactory spectral decomposition was obtained. Although, it may be a serpentine (SEM, TEM
16 analyses), no phase from the database can be associated to the experimental spectra. In
17 conclusion, two independent analytical techniques demonstrate that the whole eCP layers of
18 P285NH and Armco consist of precipitated Fe-Si-O phases identified as smectite (assimilated
19 to nontronite) and serpentine.
20
21
22
23
24
25
26
27
28
29

30 Discussion

31
32 To summarise the experiments and results, two metallic substrates, a ferritic-pearlitic steel
33 (P285NH) and a pure ferrite (Armco) were corroded during 720 h in MX80 bentonite medium
34 with a synthetic water simulating the Cox pore water in equilibria with argillite. Carbonate
35 species were not added to the experiment in order to study the silicate contribution in the
36 corrosion processes. Due to their absence, the experiment is made without pH buffer, which
37 could also affect the silicate contribution. As there is no pH buffer, the pH of the solution depend
38 on the pH of H₂O, which varies with the temperature. At 120°C, the pH of a Fe-H₂O system is
39 expected to be around 5.95 [40].
40
41
42
43
44
45
46
47
48
49
50
51
52
53
54
55
56
57
58
59
60

1
2
3 The CPL cross-sections of both samples were characterized with a multiscale analytical
4 methodology that revealed similar corrosion facies made of a bi-layer structure. The inner layer
5 is made of a compact and continuous oxide layer, which is adherent to the metallic substrate.
6
7 The external one, made of iron-rich phyllosilicates, is porous and not adherent to the inner layer.
8
9 A schematic illustration of the CPL morphology and structure is presented on figure 8
10
11 depending on the metal microstructure.
12

13 14 1. iCP : magnetite 15

16 Magnetite Fe_3O_4 was identified by Raman spectroscopy in contact with both metallic
17 surfaces. The oxide is present as a continuous layer of several hundreds of nanometers to,
18 locally, up to 25 μm around the metallic substrate. The oxide layer appears adherent to the
19 metal, nano-crystallized, compact with no visible porosity even at nanoscale. The metal
20
21 microstructure does not influence the nature, crystallinity and compactness of the iCP.
22
23
24

25
26 The magnetite layer morphology differs in P285NH and Armco samples. For P285NH,
27 Figure 2C clearly shows that local penetrations in the metal are observed through pearlite
28 grains. Although not all of the pearlite grains are associated with such penetrations. This
29 suggests the presence of local galvanic coupling on perlite grains on the sample [41]. For some
30 pearlite grains, coupling occurs between the ferrite lamellas and the cementite lamellas as both
31 components are electrical conductors. Ferrite from pearlite grains is oxidized while cementite
32 acts as a cathode where water reduction can occur, promoting an enhanced corrosion current
33 [42]. Thus, cementite runs as a cathodic site and the consequence is the heterogeneous thickness
34
35 of the magnetite layer.
36
37
38
39
40

41
42 For Armco, some local penetrations are also present but are significantly rarest (maximum
43 three per cross section of diameter 2.5 cm). These later can be related either to the metal
44 microstructure or to stochastic effects of the corrosion propagation. To conclude, the metal
45
46 microstructure influences the morphology and thickness of the iCP. The presence of pearlite in
47
48 the metal microstructure favours local penetration and heterogeneous thickness of the iCP.
49
50

51 The presence of magnetite at the M/CPL interface was already demonstrated in several
52 studies of steel corrosion in Cox medium [3–5,7,9,13] as well as in MX80 silicate environment
53 media [11,12]. In the literature, when studied at a nanoscale, the oxide layer appears with
54
55 thickness ranging from several dozen to several hundred of nm [43].
56
57
58
59
60

1
2
3 Two hypotheses can be considered for magnetite formation. The first one assumes that
4 magnetite formation occurs by co-precipitation of Fe^{3+} and Fe^{2+} either directly [44] or by
5 Schikorr reaction [45]. Magnetite would then form on the surface of the metal. However, E-pH
6 diagram of Fe-H₂O system shows that between 100 and 150°C, at pH less than 6, magnetite is
7 not stable [46]. Note that these diagrams do not include local pH variation around the metallic
8 samples.
9

10
11
12
13
14 The second one assumes that the oxide layer grows to the detriment of metal by solid-state
15 diffusion of oxygen as stated in the PDM and DPCM model [47,48]. With this hypothesis, the
16 formation of the oxide layer is linked to a steel passive layer growth [15]. The higher oxide
17 thickness measured in this experiment compared to simulation [15] and other experimental
18 studies [43,49] may be linked to the slow kinetics of montmorillonite dissolution [50], which
19 gives time for magnetite to grow.
20
21
22
23

24
25 In corrosion modelling, the sum of the anodic and cathodic current must be null ($j_e + j_{\text{Fe}^{III}} + j_{\text{vo}} = 0$). This is the coupled current condition at the $\alpha\text{-Fe}/\text{Fe}_3\text{O}_4$ interface (Fig. 9B). In
26 presence of pearlite grains, cementite is known as preferential cathodic sites i.e. the kinetic
27 constant of water reduction on cementite is higher than on magnetite [51]. Then, electron
28 current runs through cementite since the water reduction at the cementite/H₂O interface is faster
29 than at the magnetite/H₂O interface (Fig. 9A). Thus, the coupled current condition is no more
30 fulfilled at the $\alpha\text{-Fe}/\text{Fe}_3\text{O}_4$ interface. These preferential cathodic paths will activate the
31 oxidation of the $\alpha\text{-Fe}/\text{Fe}_3\text{O}_4$ interface between the cementite lamellas. This induce
32 heterogeneous corrosion. In presence of pearlite grains, corrosion of $\alpha\text{-Fe}$ runs like in « anodic
33 potentiostatic mode » (anodic enhancement) since all or a major part of the electronic current
34 doesn't cross the magnetite layer. Thus, the electrochemical condition (coupled current
35 equation) at the $\alpha\text{-Fe}/\text{Fe}_3\text{O}_4$ interface is not the same with and without cementite in the metal
36 microstructure.
37
38
39
40
41
42
43
44
45
46
47

48
49 Whatever the formation process, in liquid [44] or in solid state [52], the magnetite grains
50 crystallinity is not affected by this corrosion mechanism. As no porosity was observed on the
51 oxide layer at nanoscale, its water permeability can be questioned as well as its impact on the
52 corrosion rate.
53
54
55

56 57 58 2. eCP : Fe-rich phyllosilicate 59 60

1
2
3 For Armco and P285NH, the eCP differs from the iCP by the presence of Si. Up to the
4 magnetite layer, a diffuse, heterogeneous and very porous area containing iron rich silicate is
5 observed on SEM-EDS images. The comparison between XANES reference spectra of MX80
6 bentonite, montmorillonite and quartz (Fig. 7A) with spectrum acquired around the metallic
7 sample shows spectral differences. Thereby, phases observed in the eCP correspond to the
8 transformation of MX80 bentonite from the environment that have incorporated iron ions to
9 form iron-rich phyllosilicate: nontronite-like smectite, and serpentine type. Phyllosilicate
10 formation depends on geochemical parameters such as (but not limited to) temperature,
11 pressure, pH, oxic/anoxic medium, and Fe/clay ratio. Serpentine and/or smectite formation was
12 already observed in steel/clay interaction experiments [3,5,31,38,53–56]. Literature suggests a
13 competition between these two groups. For example, Wyoming bentonite aging for several
14 months in contact with iron up to 150°C under neutral pH, resulted in the formation of
15 serpentines for an iron/clay mass ratio > 0.5 [31]. However, for a mass ratio equals to 0.1, and/or
16 under alkaline conditions (pH = 10-12), smectite were identified. Other results, obtained with
17 an iron/clay mass ratio higher than 0.2 at 80°C in presence of FoCa7 bentonite, likewise hinted
18 at smectite transformation to serpentines [55]. Indeed, natural or synthetic smectites (nontronite
19 in particular) are preferentially formed at lower temperatures, neutral pH in reducing conditions
20 [22,38,56,57], and are destabilized above 80°C [54,58,59]. Furthermore, their destabilization
21 was systematically observed for pH higher than 7 at 80°C, in Fe/clay ratio equals to 1 [18].
22 However, whatever the amount/nature of precipitated phyllosilicate, the formation of such
23 family of phases leads to a local pH decrease [60–62]. Hence, the following of the three
24 parameters: temperature, pH and Fe/clay ratio controls smectite/serpentine transformation. In
25 the present study, both serpentine and smectite neoformation were identified in P285NH and
26 Armco.
27
28
29
30
31
32
33
34
35
36
37
38
39
40
41
42
43
44

45 The thickness of the iCP as well as the porosity and poorly adherent properties of the eCP
46 contrast with experiments where the corrosion environment contain carbonate competing with
47 silicate. Indeed, in these studies, it seems that Si-rich phases form closer to the metal interface
48 than Fe carbonate such as siderite or chukanovite, which could explain their compactness [3–
49 5,7,10]. The absence of carbonate in the environment precludes the formation of a carbonate
50 layer such as siderite that could tend to favour the formation of a fully compact CPL from the
51 early stages of corrosion.
52
53
54
55
56
57

58 Smectite is a swelling clay [63], which could influence ion exchange. After 720 h
59 experiment, due to its porous and poorly adherent properties, smectite would not influence
60

1
2
3 diffusion processes. The oxide inner layer seems compact and adherent to the metal, which may
4 have an impact on the corrosion mechanism. Further analysis of these corrosion products, for
5 example a D₂O immersion [64], may help to better identify their properties in the light of
6 diffusion processes, specifically for the magnetite layer.
7
8
9

10 **Conclusion**

11
12
13 In this study, the CPL formed at the interface of two metallic substrates in contact with
14 MX80 bentonite was characterized at the micro- and nano-scales. The CPL is made of a
15 magnetite-rich iCP and a Fe-rich phyllosilicate-rich eCP for both substrates. The metal
16 microstructure has an impact only on the iCP morphology.
17
18
19

20
21 The magnetite layer appears continuous with 500 nm average thickness and variations
22 of thickness up to 25 µm related to metal microstructures, in particular with pearlite grains for
23 P285NH. Its polycrystalline nature was highlighted with nanometric grains diameters. The
24 magnetite layer is compact, non-porous at nanoscale and adherent to the metal. Several
25 hypotheses on its formation were discussed.
26
27
28

29
30 Moreover, two types of Fe-rich phyllosilicates coexist in a porous and poorly adherent eCP:
31 smectite (nontronite type) and serpentine. Smectite is swelling clay that could reduce the
32 diffusion processes between iron and its environment. However, after 720 h experiment, the
33 eCP morphology may enable easy ionic flux from the environment to steel.
34
35
36

37
38 The morphology of the CPL is modified compared to CPL that formed in presence of
39 carbonate / silicate competition, probably because of the absence of carbonate buffer and iron
40 carbonate formation. The presence of carbonate leads to a more compact CPL around the
41 metallic substrate, which may help to reduce the interaction between steel and its environment
42 from the early stages of corrosion. However, this silicate environment favours the magnetite
43 growth. Further study of the CPL water permeability would evidence the impact of these phases
44 on the ionic exchanges between steel and the corrosion environment.
45
46
47
48

49 **Acknowledgements**

50
51 This work was partially supported by the ANR funding Investissements d'avenir ANR-11-
52 EQPX-0020 (Equipex GENESIS), by the Fonds Européen de Développement Régional and by
53 the Région Basse-Normandie.
54
55

56
57 The CLS is supported by NSERC, CIHR, NRC, the Province of Saskatchewan, WEDC and the
58 University of Saskatchewan.
59
60

References

- [1] ANDRA report, **2015**.
- [2] ANDRA report, **2005**.
- [3] M.L. Schlegel, C. Bataillon, K. Benhamida, C. Blanc, D. Menut, J.-L. Lacour, *Appl. Geochem.* **2008**, *23*, 2619.
- [4] M.L. Schlegel, C. Bataillon, C. Blanc, D. Prêt, E. Foy, *Environ. Sci. Technol.* **2010**, *44*, 1503.
- [5] M.L. Schlegel, C. Bataillon, F. Brucker, C. Blanc, D. Prêt, E. Foy, M. Chorro, *Appl. Geochem.* **2014**, *51*, 1
- [6] P. Le Pape, C. Rivard, M. Pelletier, I. Bihannic, R. Gley, S. Mathieu, L. Salsi, S. Migot, O. Barres, F. Villiéras, N. Michau, *Appl. Geochem.* **2015**, *61*, 62.
- [7] M.L. Schlegel, S. Necib, S. Daumas, C. Blanc, E. Foy, N. Trcera, A. Romaine, *Corr. Sci.* **2016**, *109*, 126.
- [8] S. Necib, Y. Linard, D. Crusset, N. Michau, S. Daumas, E. Burger, A. Romaine, M.L. Schlegel, *Cor. Sci.* **2016**, *111*, 242.
- [9] F. Bourdelle, R. Mosser-Ruck, L. Truche, C. Lorgeoux, I. Pignatelli, N. Michau, *Chem. Geol.* **2017**, *466*, 600.
- [10] M.L. Schlegel, S. Necib, S. Daumas, M. Labat, C. Blanc, E. Foy, Y. Linard, *Corr. Sci.* **2018**, *136*, 70.
- [11] N.R. Smart, A.P. Rance, L. Carlson, L.O. Werme, *Mater. Res. Soc. Symp, Proc.* **2006**, 932, 197.
- [12] L. Carlson, O. Karnland, V.M. Oversby, A.P. Rance, N.R. Smart, M. Snellman, M. Vähänen, L.O. Werme, *Phys. Chem. Earth.* **2007**, *32*, 334.
- [13] G. de Combarieu, P. Barboux, Y. Minet, *Phys. Chem. Earth.* **2007**, *32*, 346.
- [14] G. Montes-H, N. Marty, B. Fritz, A. Clement, N. Michau, *Appl. Clay Sci.* **2005**, *30*, 181.
- [15] C. Bataillon, F. Bouchon, C. Chainais-Hillairet, J. Fuhrmann, E. Hoarau, R. Touzani, *J. Comput. Phys.* **2012**, *231*, 6213.
- [16] R. Barker, D. Burkle, T. Charpentier, H. Thompson, A. Neville, *Corr. Sci.* **2018**, *142*, 312.
- [17] D. Crusset, Y. Linard, C. Martin, N. Michau, S. Necib, S. Schumacher, Andra Report CGRPASCM 150029. **2015**.
- [18] S. Lantenois, B. Lanson, F. Muller, A. Bauer, M. Jullien, A. Plançon, *Clays Clay Miner.* **2005**, *53*, 597.

- 1
2
3 [19] B. Lanson, S. Lantenois, P.A. van Aken, A. Bauer, A. Plançon, *Am. Mineral.* **2012**,
4 97, 864.
5
6 [20] C. Rivard, M. Pelletier, N. Michau, A. Razafitianamaharavo, M. Abdelmoula, J.
7 Ghanbaja, F. Villiéras, *Clays Clay Miner.* **2015**, 63, 290.
8
9 [21] E.C. Gaucher, C. Tournassat, F.J. Pearson, P. Blanc, C. Crouzet, C. Lerouge, S.
10 Altmann, *Geochim. Cosmochim. Acta.* **2009**, 73, 6470.
11
12 [22] C. Carrière, P. Dillmann, E. Foy, D. Neff, J.J. Dynes, Y. Linard, N. Michau, C.
13 Martin, *Corr. Sci.* **2019**, 158, 108104.
14
15 [23] P. Dillmann, S. Gin, D. Neff, L. Gentaz, D. Rebiscoul, *Geochim. Cosmochim. Acta.*
16 **2016**, 172, 287.
17
18 [24] C. Rivard, E. Montargès-Pelletier, D. Vantelon, M. Pelletier, C. Karunakaran, L.J.
19 Michot, F. Villieras, N. Michau, *Phys. Chem. Miner.* **2013**, 40, 115.
20
21 [25] D.L.A. de Faria, S. Venâncio Silva, M.T. de Oliveira, *J. Raman Spectrosc.* **1997**, 28,
22 873.
23
24 [26] M.L. Schlegel, C. Martin, F. Brucker, C. Bataillon, C. Blanc, M. Chorro, P. Jollivet,
25 *Appl. Geochem.* **2016**, 70, 27.
26
27 [27] M.L. Schegel, M. Sennour, C. Carrière, F. Martin, M. Fenart, J. Varlet, C. Blanc, P.
28 Dillmann, D. Neff, J.J. Dynes, EUROCORR'17, Prague, Czech Republic, 3 - 7 September 7,
29 **2017**, pp 1-13
30
31 [28] O. Grauby, S. Petit, A. Decarreau, A. Baronnet, *Eur. J. Mineral.* **1994**, 6, 99.
32
33 [29] H. Changela, J. Bridges, *Meteorit. Planet. Sci.* **2010**, 45, 1847.
34
35 [30] D.M. Moore, J. Hower, *Clays Clay Miner.* **1986**, 34, 379.
36
37 [31] R. Mosser-Ruck, M. Cathelineau, D. Guillaume, D. Charpentier, D. Rousset, O.
38 Barres, N. Michau, *Clays Clay Miner.* **2010**, 58, 280.
39
40 [32] C. Carrière, F. Mercier, M. Bouttemy, E. Foy, X. Crozes, A. Etcheberry, D. Neff, I.
41 Monnet, P. Dillmann, *J. Electron Spectros. Relat. Phenomena.* **2019**, 235, 51.
42
43 [33] L.J. Hicks, J.C. Bridges, S.J. Gurman, *Geochim. Cosmochim. Acta.* **2014**, 136, 194.
44
45 [34] F.J. Huertas, S. Fiore, J. Linares, *Clay Miner.* **2004**, 39, 423.
46
47 [35] D. Li, G.M. Bancroft, M.E. Fleet, X.H. Feng, *Phys. Chem. Miner.* **1995**, 22, 115.
48
49 [36] G. de Combarieu, M.L. Schlegel, D. Neff, E. Foy, D. Vantelon, P. Barboux, S. Gin,
50 *Appl. Geochem.* **2011**, 26, 65.
51
52 [37] L.A. Giannuzzi, R. Geurts, J. Ringnalda, *Microsc. Microanal.* **2005**, 11, 828.
53
54 [38] V.C. Farmer, G.S.R. Krishnamurti, P.M. HtJANG, *Clays Clay Miner.* **1991**, 39, 561.
55
56 [39] V.C. Farmer, D.G. Lumsdon, *Geochim. Cosmochim. Acta.* **1994**, 58, 3331.
57
58
59
60

- 1
2
3 [40] R.E. Mesmer, W.L. Marshall, D.A. Palmer, J.M. Simonson, H.F. Holmes, *J. Solution*
4 *Chem*, **1988**, *17*, 699
5
6 [41] J.-L. Crolet, N. Thevenot, S. Nestic, *Corrosion*. **1998**, *54*, 194.
7
8 [42] S. Papavinasam, *Gulf Professional Publishing*, Boston, **2014**.
9
10 [43] Y. Leon, P. Dillmann, D. Neff, M.L. Schlegel, E. Foy, J.J. Dynes, *RSC Adv*. **2017**, *7*,
11 20101.
12
13 [44] S. Laurent, D. Forge, M. Port, A. Roch, C. Robic, L. Vander Elst, R.N. Muller, *Chem.*
14 *Rev*. **2008**, *108*, 2064.
15
16 [45] V.G. Schikorr, *Z. Anorg. Allg. Chem.* **1931**, *35*, 33.
17
18 [46] J. Chivot, *Collection science et technique*, **2004**
19
20 [47] D.D. Macdonald, M. Urquidimacdonald, *J. Electrochem. Soc.* **1990**, *137*, 2395.
21
22 [48] C. Bataillon, F. Bouchon, C. Chainais-Hillairet, C. Desgranges, E. Hoarau, F. Martin,
23 S. Perrin, M. Tupin, *J. Talandier, Electrochim. Acta.* **2010**, *55*, 4451.
24
25 [49] Y. Leon, M. Saheb, E. Drouet, D. Neff, E. Foy, E. Leroy, J.J. Dynes, P. Dillmann,
26 *Corros. Sci.* **2014**, *88*, 23.
27
28 [50] O. Bildstein, L. Trotignon, M. Perronnet, M. Jullien, *Phys. Chem. Earth, Parts A/B/C.*
29 **2006**, *31*, 618.
30
31 [51] A.C. Makrides, *J. Electrochem. Soc.* **1964**, *111*, 392.
32
33 [52] N. Bertrand, C. Desgranges, D. Poquillon, M.C. Lafont, D. Monceau, *Oxid. Met.* **2010**,
34 *73*, 139.
35
36 [53] C. Rivard, M. Pelletier, N. Michau, A. Razafitianamaharavo, I. Bihannic, M.
37 Abdelmoula, J. Ghanbaja, F. Villiéras, *Am. Mineral.* **2013**, *98*, 163.
38
39 [54] I. Pignatelli, E. Mugnaioli, J. Hybler, R. Mosser-Ruck, M. Cathelineau, N. Michau,
40 *Clays Clay Miner.* **2013**, *61*, 277.
41
42 [55] M. Perronnet, M. Jullien, F. Villiéras, J. Raynal, D. Bonnin, G. Bruno, *Appl. Clay Sci.*
43 **2008**, *38*, 187.
44
45 [56] R.B. Merola, E.D. Fournier, M.M. McGuire, *Langmuir*. **2007**, *23*, 1223.
46
47 [57] H. Harder, *Chem. Geol.* **1976**, *18*, 169.
48
49 [58] J.C. Wilson, S. Benbow, H. Sasamoto, D. Savage, C. Watson, *Appl. Geochem.* **2015**,
50 *61*, 10.
51
52 [59] I. Pignatelli, F. Bourdelle, D. Bartier, R. Mosser-Ruck, L. Truche, E. Mugnaioli, N.
53 Michau, *Chem. Geol.* **2014**, *387*, 1.
54
55 [60] J.C. Fernández-Caliani, E. Crespo, M. Rodas, J.F. Barrenechea, F.J. Luque, *Clays*
56 *Clay Miner.* **2004**, *52*, 106
57
58 [61] S. Hillier, B. Velde, *Clay Miner.* **1992**, *27*, 475.
59
60

[62] B.M.J. Thien, N. Godon, A. Ballester, S. Gin, A. Ayrat, *J. Nucl. Mater.* **2012**, 427, 297.

[63] D.A. Laird, *Appl. Clay Sci.* **2006**, 34, 74.

[64] M. Saheb, P. Berger, L. Raimbault, D. Neff, P. Dillmann, *J. Nucl. Mater.* **2012**, 423, 61

Table 1- Chemical composition of the two low-alloy carbon steels used in the corrosion experiment (wt. %)

Elements	C	Si	Mn	S	P	Cr	Mo	Ni	Cu	Fe
P285NH	0.15	0.25	1.03	0.001	0.006	0.081	0.021	0.067	0.073	Base
Armco	0.002	0.009	0.33	0.019	0.005	-	-	-	0.03	Base

Table 2- Chemical composition of Cox synthetic solution without carbonated compound

Compounds	Concentration [mmol.L ⁻¹]
Na ₂ SO ₄	10
KCl	0.96
CaCl ₂	10
MgCl ₂	2.5
SrCl ₂	0.14
NaCl	14.7

Table 3- Mineral composition of MX80 Bentonite

Mineral	Dry proportion (vol. %)
Na/Ca-Montmorillonite	84.35
Quartz	7.03
Albite	3.49
Biotite	2.78
Microdine	1.07
Calcite	0.97

Pyrite 0.31

Table 4- Inter-planar distance (d) of magnetite Fe_3O_4 extracted from the diffraction pattern of Fig. 4A

d_{hkl} (Å)
4.9
3.0
2.6
2.1
1.7
1.6
1.5

Table 5- Chemical composition of Region of Interest (RoI) identify on Fig. 5 for P285NH (1 and 2) and Armco (3 and 4), at. %

RoI	.1	.2	.3	.4
O	56	61	60	66
Si	18	21	18	21
Fe	17	5	17	6
Al	7	10	4	7
Mg	1	1.5	1	1
Na	1	1.5	n.d.	1

Table 6- Best FIT parameters for the linear regression performed on XANES Si K-edge spectrum

Sample	Contribution for linear regression	R^2	χ^2
P285NH	89% nontronite + 11% SiO_2	0.99	0.01
Armco	93% nontronite + 7% SiO_2	0.99	0.01

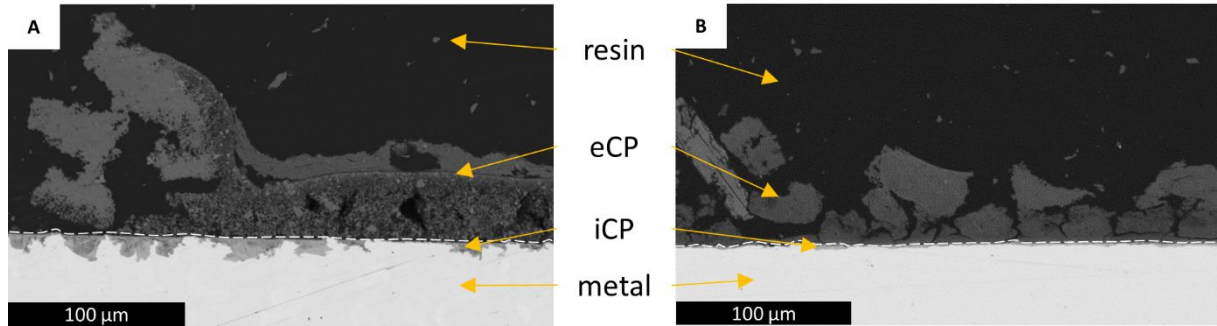


Figure 1- SEM micrographs in BSE obtained on P285NH (A) and Armco (B) cross-section. The white lines correspond to the interface between the iCP and the eCP

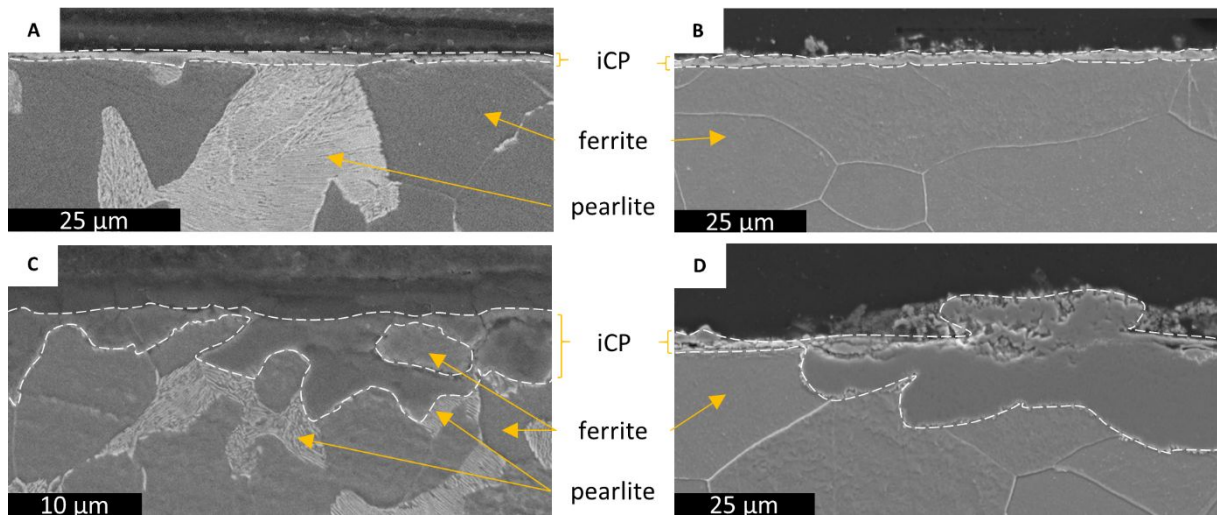


Figure 2- SEM micrographs in SE obtained at the M/CPL interfaces evidencing different oxide layer thicknesses on P285NH (A-C) and Armco (B-D). The white lines delimit the iCP.

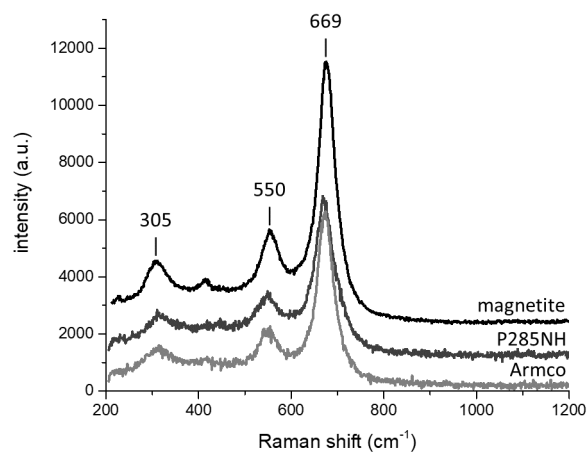


Figure 3- Raman spectra acquired at the M/CPL interfaces in the iCP of P285NH and Armco

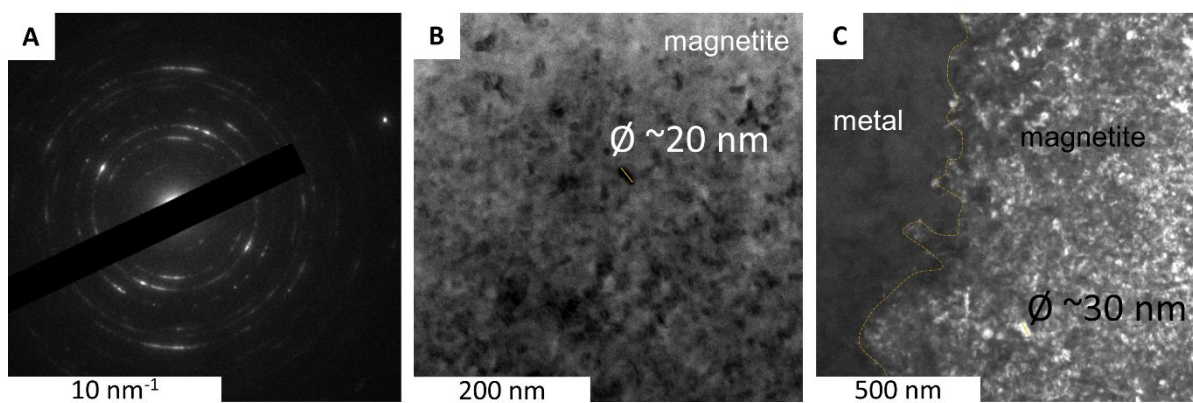


Figure 4- Electron diffraction pattern associated to the magnetite from Armco (A) and TEM images of the magnetite strip: P285NH (B) and Armco (C). The yellow line delimit the metal/oxide interface.

1
2
3
4
5
6
7
8
9
10
11
12
13
14
15
16
17
18
19
20
21
22
23
24
25
26
27
28
29
30
31
32
33
34
35
36
37
38
39
40
41
42
43
44
45
46
47
48
49
50
51
52
53
54
55
56
57
58
59
60

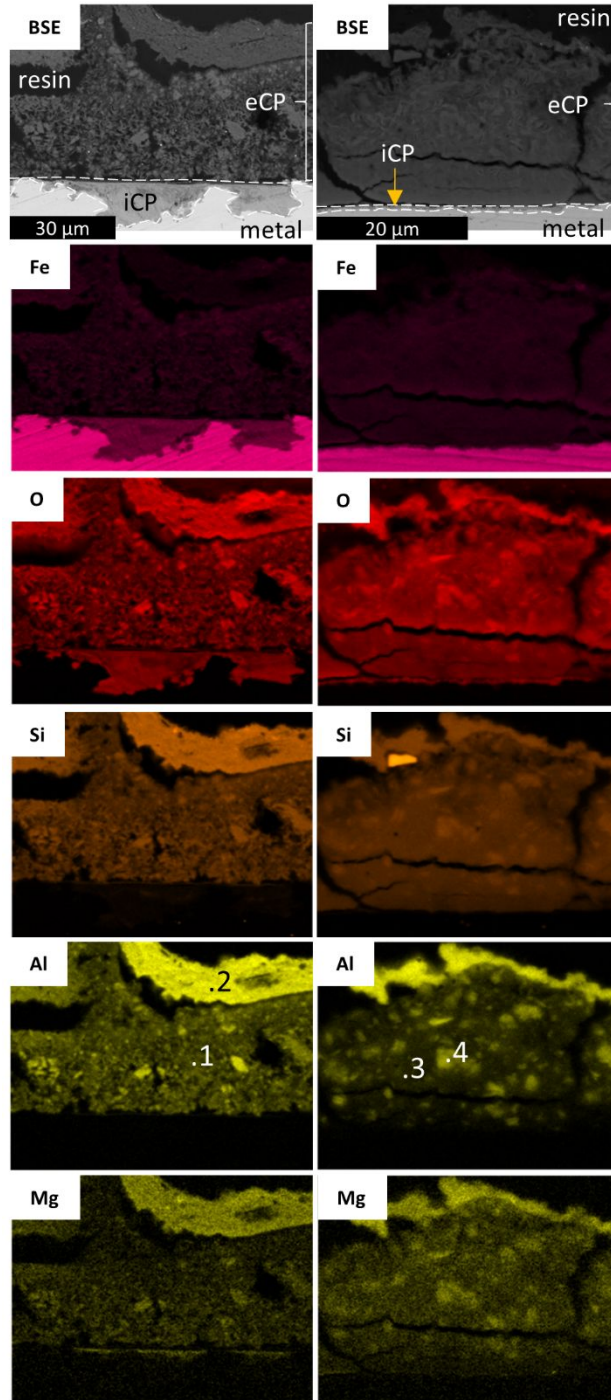


Figure 5- SEM micrographs in BSE and EDS chemical mapping of the corrosion layer on P285NH (left) and Armco (right). The white lines delimit the iCP.

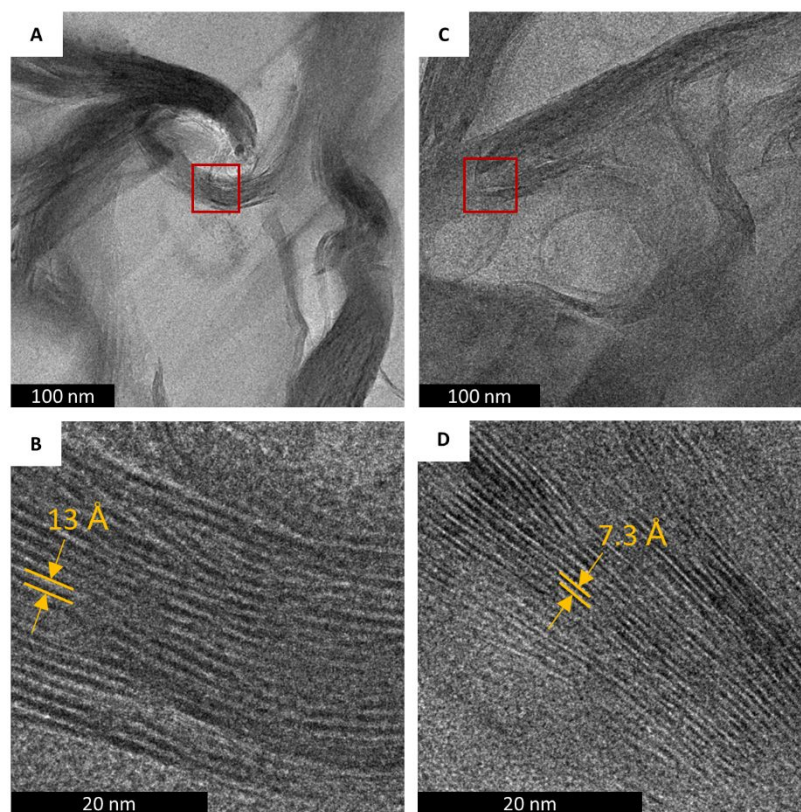


Figure 6- HR-TEM micrographs obtained on P285NH sample in eCPL. B and D correspond to zoom obtained on A and C, respectively

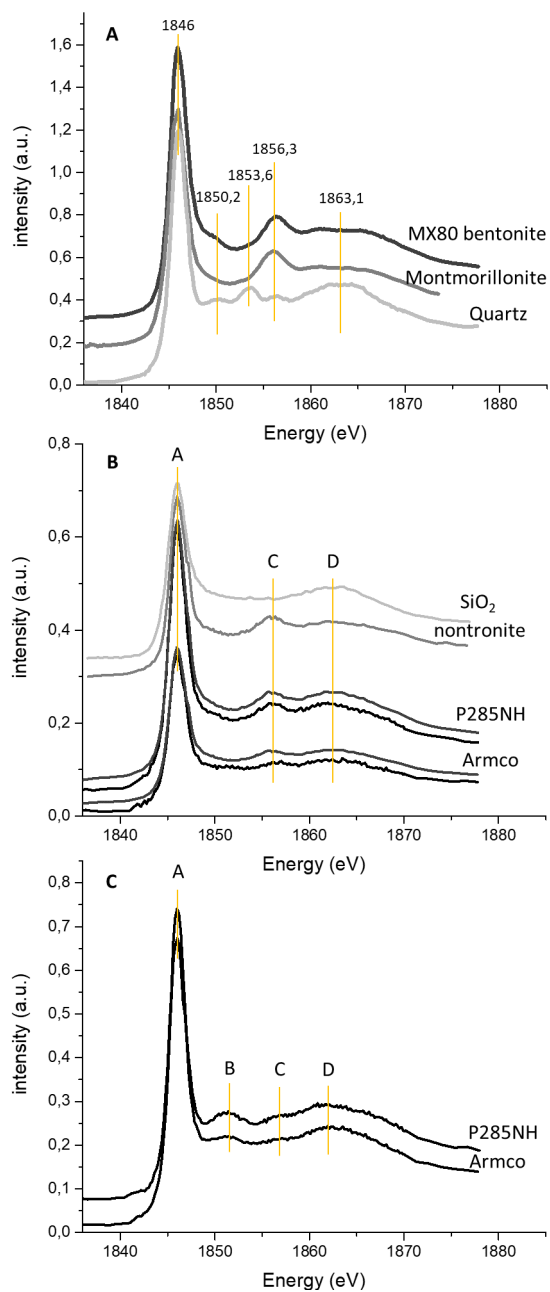


Figure 7- XANES Si K-edge reference spectra obtained on MX80 bentonite, montmorillonite, quartz (A) and experimental spectra (black) acquired on the eCP of P285NH and Armco (B and C) with associated fit, nontronite and amorphous SiO₂ (grey).

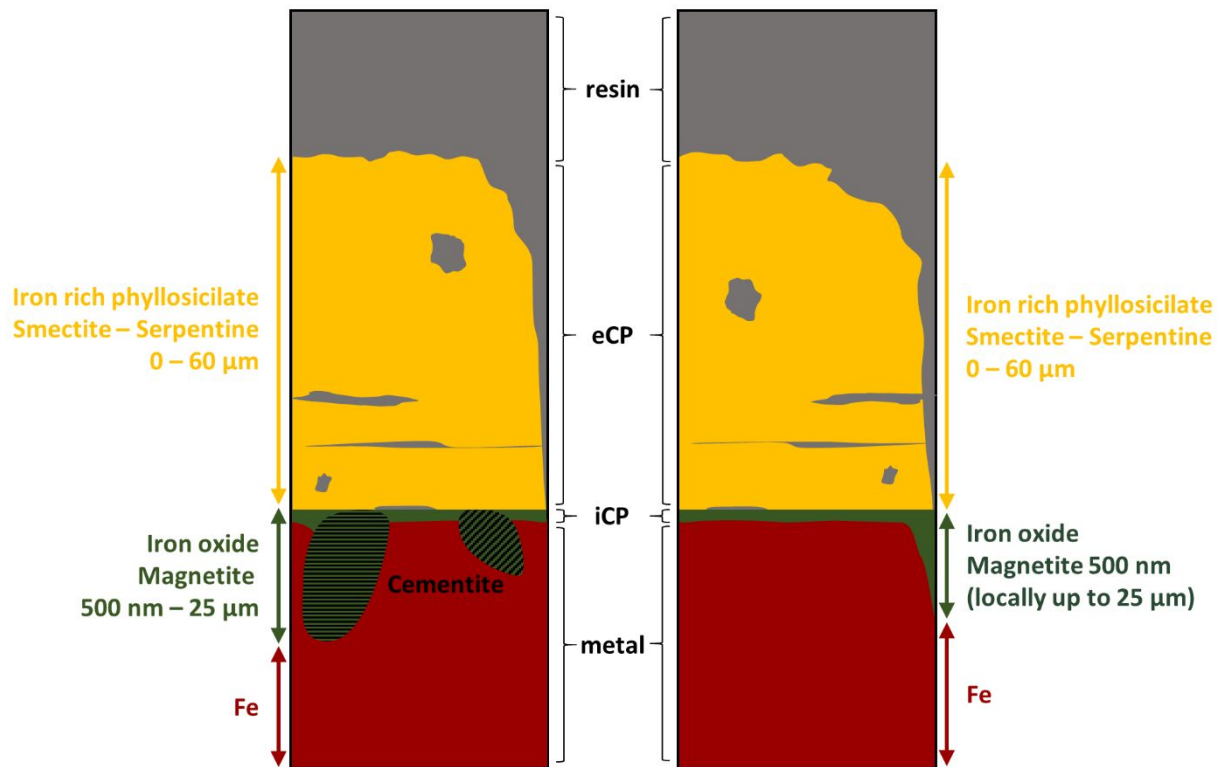


Figure 8- Schematic representation of the iron–clay corrosion interface after 720 h at 120 °C for P285NH (left) and Armco (right)

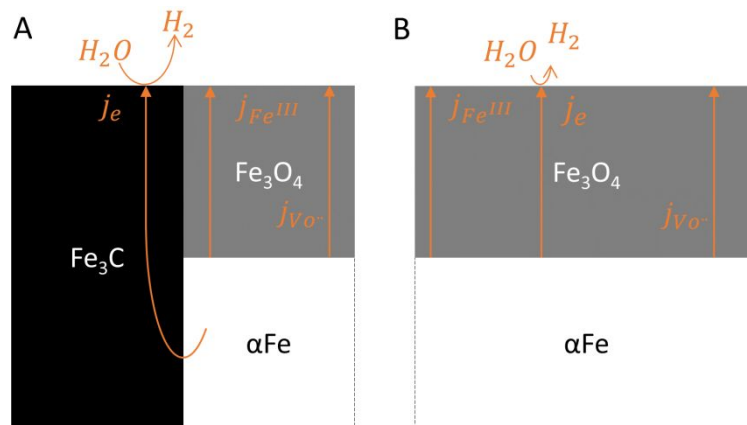


Figure 9- Schematic representation of the diffusion process with (A) and without (B) cementite with j the current of electron e , Fe^{III} and oxygen vacancy $vo\cdot$